POLITECNICO
MILANO 1863

SCUOLA DI INGEGNERIA INDUSTRIALE
E DELL'INFORMAZIONE

Understanding friction drag reduction via synthetic forcing

Tesi di Laurea Magistrale in
Aeronautical Engineering - Ingegneria aeronautica

Andrea Conforti, 10580466

Advisor:
Prof. Maurizio Quadrio

Co-advisors:
Ing. Federica Gattere
Dott. Alessandro Chiarini

Academic year:
2022-2023

Abstract: The aim of this study is to advance understanding of the friction drag reduction phenomenon induced by transverse forcing. The traditional wall oscillation technique generates a transverse boundary layer, known as the Stokes layer, in which the velocity profile is analytically described by the solution of the second Stokes problem. However, it is challenging to understand whether the reduction in friction is mainly determined by the wall-normal spatial characteristics of the Stokes layer velocity profile or by its temporal variation, as both are related to a previously chosen value of the period of wall oscillation T. A novel approach is suggested that imposes the transverse velocity profile directly on the flow, keeping the wall still. Through the proposed method, the spatial and temporal variations are separated into two parameters: one that measures the wall-normal thickness of the spanwise velocity profile and the other that represents its temporal period of oscillation. This allows for the evaluation of their separate influence on friction drag reduction and gain a more comprehensive understanding of the underlying physics.
A DNS-based parametric study reveals that the temporal variation of the Stokes layer dominates the skin friction reduction, while the spatial variation contributes to a lesser extent. The optimal period of wall oscillation for maximum friction drag reduction is found to be smaller than the traditionally chosen value in wall oscillation techniques. Evidence is presented through the study of Reynolds stresses and the behavior of tracer particles varying with the two parameters on why some velocity profiles are more efficient in providing greater friction reduction. Specifically, certain values of the Stokes layer oscillation period are found to be more effective in reducing vertical velocity fluctuations, thus reducing turbulent activity within the transverse boundary layer.

Key-words: Drag reduction, spanwise forcing, Stokes layer, tracer particles

1. Introduction

The reduction of drag and improvement of flow efficiency have been a long-standing objective in fluid dynamics. One drag reduction approach that has gained significant attention in past years is the oscillating wall technique. First introduced by [25] for a turbulent channel flow, it involves periodic perturbations of the walls to modify the flow patterns and reduce skin-friction drag. The wall movement is described as a sinusoidal function:

$$W(y=0,t) = A\sin\left(\frac{2\pi}{T}t\right), \tag{1}$$

where $W(0,t)$ represents the spanwise component of the mean velocity vector at the wall, t is time, y is the wall-normal coordinate, A is the oscillation amplitude, and T is the oscillation period.
The flow over the oscillating walls results from the combination of two simpler flows: a canonical turbulent channel flow in the streamwise direction and an oscillating boundary-layer flow in the transversal (spanwise) direction, induced by the wall movement itself.
The spanwise velocity profile $W(y,t)$ within the latter is described by the analytical laminar solution of the second Stokes problem, also known as the Stokes layer [39, 40]:

$$W(y,t) = A\exp\left(-\sqrt{\frac{\pi}{T\nu}}y\right)\sin\left(\frac{2\pi}{T}t - \sqrt{\frac{\pi}{T\nu}}y\right). \tag{2}$$

An important quantity when Eq. (2) is taken into account is the so-called Stokes layer thickness $\delta = \sqrt{T\nu/\pi}$ (where ν is kinematic viscosity of the fluid), which is physically defined as the wall-normal location at which the mean spanwise velocity W reduces to $\exp^{-1} A$, and it is an indicator of how thick or thin such Stokes layer is. Since δ is explicitly dependent on T, once the wall oscillation period is chosen, the spatial variation of the velocity profile within the transverse boundary layer is set. According to [9], the analytical laminar solution of the second Stokes problem (Eq. (2)) is an excellent solution also for the turbulent case.
Although there is not yet a consensus on the mechanism by which this type of forcing leads to skin-friction drag reduction, extensive literature [see 42, and references therein] provides ample evidence of its positive effects through both numerical simulations and experimental studies.
The effects of wall motion (Eq. (1)) have been studied for a wide range of oscillation periods, amplitudes and Reynolds numbers. For example [7] showed, through Direct Numerical Simulation (DNS) of turbulent channel flow, that the greatest drag reduction occurs when the oscillation period T^+ is near 100: at such T^+ and $A^+ = 20$, drag reduction percentages of 44.5%, 39.2% and 34.1% were achieved at Reynolds numbers $Re_\tau = 100, 200$ and 400, respectively (the $+$ superscript stands for quantities that have been made dimensionless using inner variables, specifically the friction velocity of the reference case $u_{\tau,0}$). In a later study, [38] performed a review of DNS and experimental research, founding that the optimum period at fixed A^+ is in the range of $T^+ = 100 - 125$. Similar results were found by [13], since they established that the ideal oscillation period was $T^+ = 100$ at $Re_\tau = 200$ and $T^+ = 90$ at $Re_\tau = 1000$. This shows how the optimal $T^+ = T^+_{opt}$ does not change much with changes in the Reynolds number, even when Re_τ becomes high enough to reveal clear large-scale patterns of the energetic outer log-layer structures, also known as "super-streaks" [18], which are clearly visible on the small-scale near-wall structures [19].
Despite a large number of studies, the way the Stokes Layer positively interacts with the turbulent structures is not fully understood yet. According to [1] and [27], drag reduction mechanism is linked to the presence of Quasi-Streamwise Vortices (QSVs) and longitudinal low-speed streaks, which play a crucial role in the regeneration cycle of near-wall turbulence [21, 44]. Modifying this cycle by manipulating QSVs and streaks is generally acknowledged [10] as the basis for the drag-reducing effectiveness of the Stokes layer. As documented, the dipendence of drag reduction on parameter T is certain, whereas uncertain is whether T directly influences drag reduction due to the particular temporal frequency $\omega = 2\pi/T$, or whether the effect is due to the resulting value of $\delta(T)$, which allows the Stokes layer to penetrate in the right (in terms of reducing drag) wall-normal region to effectively breaks the connection between streaks and QSVs.
Over the years, several theories have been proposed to explain the reason why the specific value of $T^+ = 100$ is optimal for reducing drag, and this topic has been under discussion for quite some time. As reported in [38], when the oscillation period T^+ is close to the optimal value, it matches the double of the typical survival time of statistically signficant turbulent structures [37], resulting in the effective disruption of streaks. This leads to a more uniform near-wall flow and a reduction in turbulence intensity. On the other hand, when T^+ exceeds the optimal value, the near-wall streaks have sufficient time to evolve before the next cycle of the Stokes layer, leading to a readaptation of near-wall turbulence to its natural state and restoring the unperturbed value of the friction coefficient. However, when T^+ is further increased beyond 100, consequently $\delta^+(T^+)$ increases as well, and the Stokes layer penetrates into the buffer layer and eventually propagates into the turbulent layer, increasing turbulence production above the viscous sublayer and negating the beneficial effects within the latter.
In order to explore the bond between the Stokes layer and turbulent structures, it is advantageous to conduct a statistical comparison of the behavior of drag-reduced flows with the refencence one. Previous studies, such as [3] and [16], have utilized single-point statistics to compare the budget of turbulent kinetic energy in natural and controlled flows, specifically in the context of spanwise oscillating walls. [47] have employed a triple decomposition of the velocity field to describe the budgets of the entire set of Reynolds stresses formed with the stochastic component of velocity. Their analysis has revealed noteworthy interactions within and among various budget terms of the stresses. As a result, investigating the changes in these stresses and their budget terms can certainly be interesting to understand the effects of spanwise forcing on the flow.
This paper examines how different parameters of the Stokes layer, namely T and δ, influence the reduction of skin-friction drag in a channel flow. The geometry of the channel is shown in Fig. 1. Section 2 describes the DNS

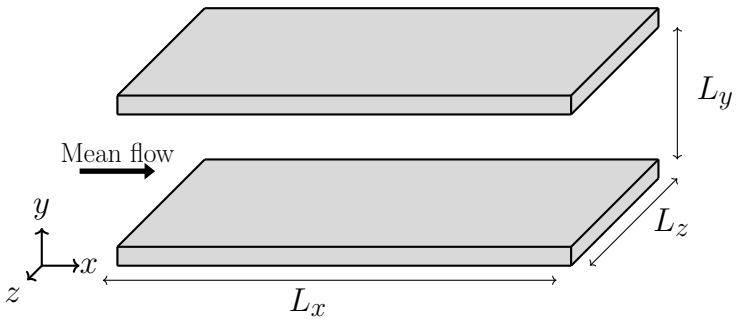

Figure 1: Schematic geometry of a plane channel flow.

code used to simulate an incompressible turbulent channel flow, including the specifics of the spanwise forcing employed. Section 3 presents the numerical outcomes of the drag reduction study, with a descriptive analysis in Section 3.1 and an investigation of the impact of forcing on the flow, by analyzing Reynolds stress budget terms in Section 3.2. This study also employs the particle tracking technique, which is introduced in Section 4, along with its computational model in Section 4.1. Finally, Section 5 conducts an analysis to understand the behavior of the flow under various forcing conditions by inserting tracer particles into the channel and investigating the existence and behavior of the shear sheltering phenomenon, which is explained in detail in Section 4.

2. Work description

2.1. Numerical method

In this study, the incompressible Navier-Stokes equations for a turbulent channel flow are solved using a computational code developed by [29]. This code utilizes two scalar equations for the wall-normal component of the velocity and vorticity vectors and eliminates the pressure by employing a method described in [26]. The DNS solver employs fourth-order-accurate compact finite-difference schemes in the wall-normal direction y and Fourier expansions in the homogeneous streamwise x and spanwise z directions, providing resolution comparable to spectral schemes while offering advantages in parallel computing. A pseudo-spectral method is utilized for evaluating the non-linear terms of the equations. In order to eliminate the related aliasing error, the number of Fourier modes is expanded by at least a 3/2 factor before transforming from Fourier space into physical space. Time integration is performed using a partially implicit approach: a second-order Crank-Nicolson scheme is used for the viscous terms, while convective terms are computed using a third-order low-storage Runge-Kutta method. The details of the DNS code Compiler and Programming Language (CPL) are explained in [28]. All simulations were carried out on the CINECA computing system (GALILEO100 cluster).

2.2. Input parameters

The simulations are performed under a Constant Flow Rate (CFR) [36] and the bulk velocity is $U_b = 2/3U_p$, where U_p is the centerline velocity of a laminar Poiseuille flow with the same flow rate. The simulations have been run at a Reynolds number $Re = U_p h/\nu = 10500$, which corresponds (in the unforced case) to $Re_\tau = u_\tau h/\nu = 400$, where h is half the distance between the channel walls, and u_τ is the friction velocity of the uncontrolled case. The size of the computational box is $(L_x, L_y, L_z) = (4\pi h, 2h, 2\pi h)$ in the streamwise, wall-normal and spanwise directions. Such computational box has been discretized with $N_y = 300$ grid points in the wall-normal direction y, and $N_x = 256$ and $N_z = 256$ Fourier modes in the x and z direction respectively, further increased by a factor of 3/2 to remove aliasing error. The streamwise and spanwise resolutions are $\Delta x^+ \approx 13$ and $\Delta z^+ \approx 6.5$, considering the additional modes used to prevent aliasing error. For the mesh in the wall-normal direction, a constant-linear nodes distribution was adopted, maintaining $\Delta y^+_{min} = 0.5$ until $y^+ < 25$, after which Δy^+ increases linearly until achieving $\Delta y^+_{max} \approx 6.2$ at the channel centerline. Each simulation has been run for 10,000 time steps with $\Delta t^+ \approx 0.15$, starting from a well-developed flow condition. The skin-friction coefficient for the unforced flow case is $C_{f,0} = 2\tau_x/(\rho U_b^2) = 6.54 \times 10^{-3}$, where τ_x is the time and space averaged (in homogeneous direction) streamwise wall-shear stress and ρ is the fluid density. This value agrees with the one estimated by the empirical formula $C_f = 0.0336 Re_\tau^{-0.273}$ given by [34]. The primary aim of this study is to investigate how the addressed spanwise forcing (further described in Section 2.3) affects the friction coefficient C_f. The friction coefficient C_f is obtained by taking the average over the entire wall surface

and time, after discarding the initial transient phase in which the flow adapts to the new forcing condition. The changes in C_f are measured as a percentage with respect to the friction coefficient of the reference case $C_{f,0}$ through DR(%) parameter, defined as follow:

$$DR(\%) = 100\frac{C_{f,0} - C_f}{C_{f,0}}, \tag{3}$$

where DR(%) corresponds to the percentage reduction in the energy required to drive the fluid in streamwise direction at a fixed flow rate (CFR).

2.3. Forcing strategy and validation

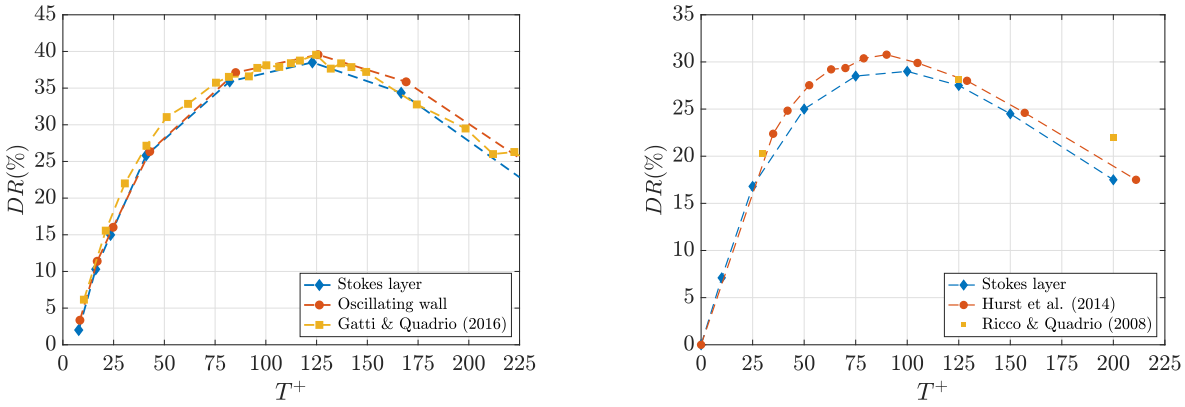

(a) (b)

Figure 2: (a) shows DR(%) results comparison between directly imposing the Stokes layer profile and oscillating wall technique for both present work and Gatti & Quadrio [14] database (at $Re_\tau = 200$). (b) shows DR(%) results comparison between directly imposing the Stokes layer profile and oscillating wall technique for both Hurst et al. [17] and Ricco & Quadrio [41] database (at $Re_\tau = 400$).

To begin, it is important to address a fundamental question regarding the relative importance of δ and T in drag reduction. In the canonical case of an oscillating wall, the transverse boundary layer is completely determined by the laminar Stokes' solution (see Eq. (2)), which is a function of T only, making it difficult to understand the interaction between turbulent structures and the velocity profile through this single parameter. In order to investigate their individual influence on drag reduction, we made δ and T independent, enforcing the Stokes layer directly to a turbulent channel flow, keeping the wall still. This was achieved through the analytical expression of the Stokes layer, in which δ is no longer a function of T and can be directly changed as an independent variable, as follow:

$$W(y,t) = A\exp\left(-\frac{y}{\delta}\right)\sin\left(\frac{2\pi}{T}t - \frac{y}{\delta}\right). \tag{4}$$

From a computational point of view, this means assigning the entire mean spanwise velocity profile $W(y,t)$ (Eq. (4)) upstream of the convolution calculations (where triadic interactions are included) at each time step, in order to ensure that the interaction of all modes occurs with the desired mean profile.
In order to verify the accuracy of this technique, we relied on simulations of the classical oscillating wall results, enforcing the laminar Stokes layer as the mean transverse velocity (Eq. (2)). The results obtained directly enforcing $W(y,t)$ were compared with oscillating wall results (see Eq. (1)) from both present work and [14] database at $Re_\tau = 200$, and very good corrispondence has been found, as shown in Figure 2a. Subsequently, when we imposed velocity profiles using the independent parameters T and δ, it was noticed that for the most impactful forcings on drag reduction, unstable relaminarization of turbulent flow [31] occurred at $Re_\tau = 200$. In order to avoid this phenomenon, the results presented in this paper will refer to simulations conducted at $Re_\tau = 400$.
Figure 2b shows the DR(%) results of our work, compared with the available oscillating walls databases at $Re_\tau = 400$. The small differences in terms of absolute value may be due to the fact that there is not a perfect correlation between the imposed laminar Stokes layer and the wall motion, although overall the results are satisfactory.

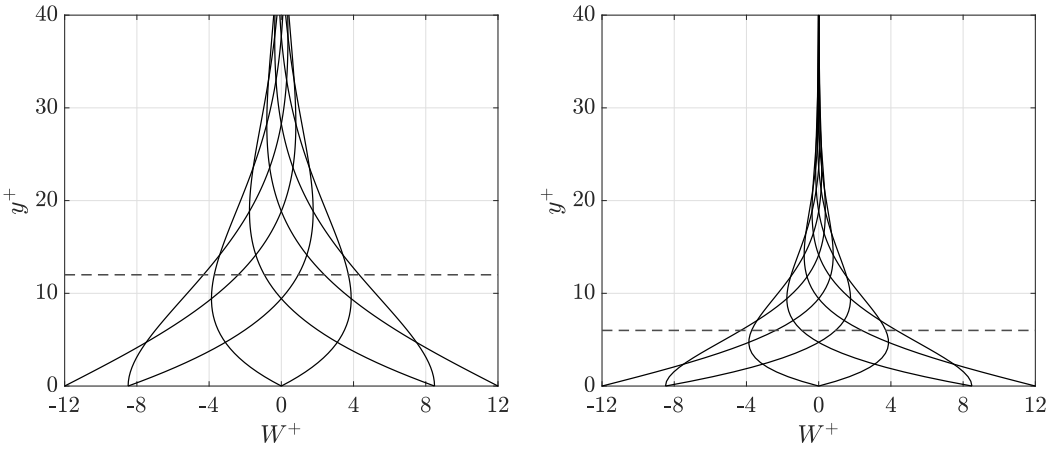

Figure 3: Comparison between two different forcing velocity profiles $W^+(y^+, t)$ for two different δ^+ ($\delta^+ = 12$ on the left and $\delta^+ = 6$ on the right), both plotted at 8 equally spaced phases in a complete temporal cycle.

The main simulations are about applying various $W(y, t)$ (Eq. (4)) for different (T^+, δ^+) pairs, and then analyzing the resulting DR(%) case by case. The selected range of oscillation period values was $T^+ = 25 - 200$, with a $\Delta T^+ = 25$ between each value. An additional value of $T^+ = 10$ was then chosen to represent a sufficiently low-period case. The range of δ^+ investigated was $\delta^+ = 2 - 20$, with a $\Delta\delta^+ = 2$, to test velocity profiles which perturbes near wall structures at different wall-normal location zones, as shown in Fig. 3. Obviously, for each value of T^+, the typical case of the canonical Stokes layer has also been simulated, namely where $\delta^+ = \sqrt{T^+/\pi}$. As a result, 92 different simulations were carried out for the different (T^+, δ^+) pairs, together with a reference simulation of the unforced flow. The forcing oscillation amplitude is set to $A^+ = 12$, that corresponds to most available database informations [13, 17].

3. Drag reduction results

3.1. Decoupled Stokes layer

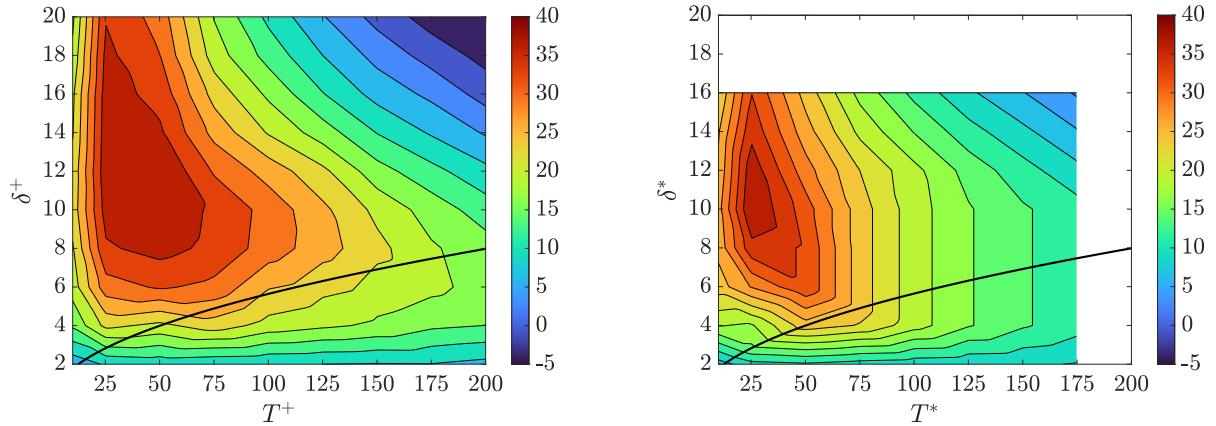

(a) (b)

Figure 4: DR(%) for different (T^+, δ^+) pairs in reference scaling (a) and (b) for different (T^*, δ^*) pairs in actual scaling (at Nominal $Re_\tau = 400$ and $A^+ = 12$). Black line is the true Stokes layer ($\delta = \sqrt{T\nu/\pi}$).

In this section, the results of the analyses just described are explored, with the aim of making a step towards a better understanding of the relationship between transverse forcing parameters (T, δ) and Drag Reduction

(DR). Through a parametric study it is attempted to understand whether it is the spatial variation of the profile (driven by δ) or its temporal oscillation (T) that plays a decisive role in DR. In this paper, all variables may be presented with (+) or (∗) superscript: the former represents quantities made dimensionless with the friction velocity of the reference case $u_{\tau,0}$, the latter of the actual drag reduced case u_τ.
From now on, we will refer to the Stokes layer resulting from arbitrarily chosen δ values as the "decoupled Stokes layer", while the Stokes layer resulting from $\delta = \sqrt{T\nu/\pi}$ will be referred to as the "true Stokes layer".
Both Figures 4a and 4b show how DR changes with different types of transverse velocity profiles imposed at the wall. The results in Fig. 4a are presented based on nominal scaled variables, while those in Fig. 4b are based on actual inner scaling. Obviously, in the latter figure, DR results are only available for a limited set of values compared to nominal scaling, since the values of T^* and δ^* are not known in advance.
To clarify, the parameter T controls how the Stokes layer behaves over time, while δ controls its behavior along the wall-normal direction. A Stokes layer with low values of both δ and T will be very thin and exhibit rapid temporal behavior, while a layer with high values of these parameters will be thicker and exhibit slower temporal behavior.
From Figure 4a, the first thing is important to note is that the well-known oscillating wall technique, which results only in velocity profiles that lie on the black line, is limiting in terms of DR, especially for $T^+ < 150$. This shows that all previous analyses which had recognized an optimal value for the forcing period $T^+ = 100$ [see 42, and references therein], were biased by the fact that a certain T^+ corresponded to a fixed δ^+, with the result that the two contributions (spatial and temporal) could not be evaluated separately and therefore in a complete and clear way. Consequently, the value of $T^+ = 100$ designated as the optimal value by an extensive literature (as underlined in Section 1), does not hold any significant meaning. The genuinely optimal periods are significally smaller, and having a fast temporal oscillation to create a thick Stokes layer shows the potential to increase DR by 40%. In particular, while with the true Stokes layer we obtain a $DR_{max}(\%) = 28.3$ for $(T^+, \delta^+(T^+)) = (100, 5.64)$, it is possible to reach a value of $DR_{max}(\%) \approx 40$ for $(T^+_{opt}, \delta^+_{opt}) = (40, 12)$ pair with the decoupled velocity profile.
Focusing initially on the oscillation period, this value of T^+_{opt} is not random or meaningless: in fact, $T^+_{opt} = 40$ had already been identified as the Lagrangian time scale representing a typical survival time of the statistically significant turbulent structures by [37]. In particular, through the integral of the autocorrelation function $R(\epsilon^+, \tau^+)$ (where ϵ^+ and τ^+ are spatial and temporal separation), they found that the life-time scale T_l for the components of velocity at $y^+ = 10$ are $T^+_{l,u} = 68$, $T^+_{l,v}$ and $T^+_{l,w} = 46$ (where u, v, and w are the velocity components in the streamwise x, wall-normal y and spanwise z directions, respectively). The time scale T^l corresponds to the entire lifespan of turbulent structures, as it measures the duration for which the signal remains correlated while in motion. It seems that when T^+ is larger than the optimum, the near-wall streaks are given enough time to establish their internal dynamics between successive Stokes layer cycles. However, when $T^+ \simeq T^+_{opt}$, the forcing time aligns with the characteristic time of streak dynamics and effectively disrupts the streaks, preventing them from adjusting to their natural life cycle.
In general, an alternative approach to explain the value of T^+_{opt} is to look at the streamwise characteristic length implied by this value of the period, obtained through the near-wall convection velocity $u^+_c = 10$ as $\lambda^+ = u^+_c \cdot T^+_{opt}$. As reported in Section 1, previous studies on the oscillating wall technique have found that $T^+_{opt} = 100$, and since the resulting $\lambda^+ = u^+_c \cdot T^+_{opt} = 1000$ matches the characteristic lenght of the longest near-wall streaks, it may be a possible explanation for that particular optimal value of the period. Anyway, once we have understood that the real $T^+_{opt} = 40$, the theoretical obtained characteristic lenght would become $\lambda^+ = u^+_c \cdot T^+_{opt} = 400$, which does not match anymore with longest streaks' lenght. Despite that, [24] has shown that the long streaks are only a by-product of the near-wall cycle and they are not an active part of the near-wall cycle. Therefore, it is possible that $\lambda^+ = 400$ corresponds to the lenght scales of the structures that are more directly involved in the near-wall cycle, and that increasing T^+ reduces the effect on the DR, because in this case the interacting structures are not directly involved in the wall cycle.
Conversely, a deeper analysis needs to be carried out to fully understand the importance of δ^+: the absolute $DR_{max}(\%)$ is obtained for $(T^+, \delta^+) = (50, 12)$, but it cannot be said that $\delta^+ = 12$ represents the optimum for all oscillation periods. Indeed, as T^+ deviates from T^+_{opt}, it can be observed that δ^+_{opt} gradually decreases (Fig. 5a). Anyway, $\delta^+_{opt} = 12$ is not an unexpected value, since it is well established that the dinamically relevant turbulent structures are located at a height of $y^+ \approx 12$ from the wall, as reported by [11]. If these specific structures are forced with T^+_{opt}, it is effective if the transverse boundary layer includes these streaks. On the other hand, if the period is far from the optimal one, the best result is obtained when the decoupled Stokes layer remains slightly closer to the wall, only tilting the near-wall structures, which seem to be much less dependent on the oscillation period value.

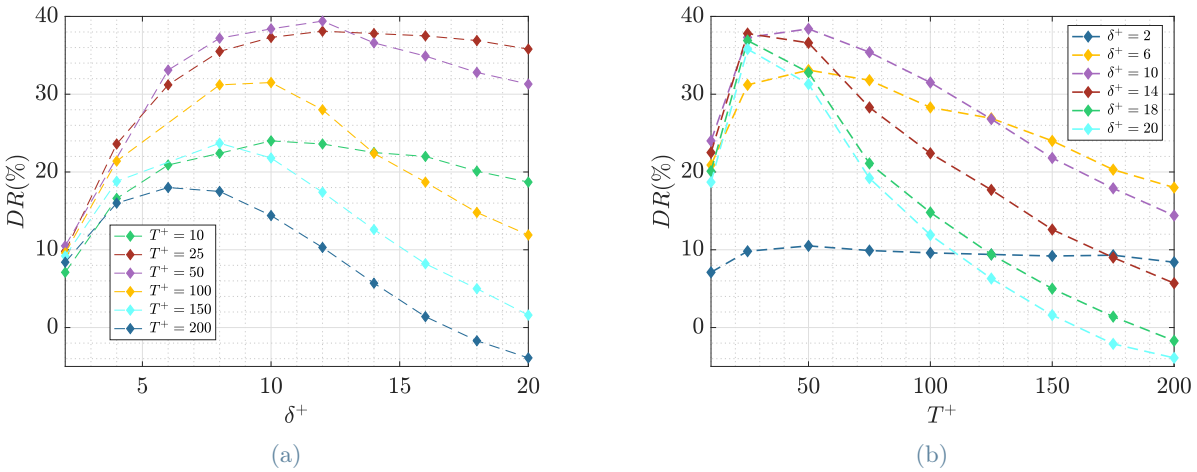

Figure 5: DR(%) as a function of δ^+ for different T^+ (a) and as a function of T^+ for different δ^+ (b). The results regards simulations conducted at Nominal $Re_\tau = 400$ and $A^+ = 12$.

This statement is confirmed by looking at the DR results for $\delta^+ = 2$ (Fig. 5b), where a sort of independence of DR with respect to T^+ is clearly visible. Similarly, a certain DR independence, this time with respect to δ^+, can be noticed for curves at very low periods as $10 \leq T^+ \leq 20$ (Fig. 5a). These observations can be explained by the fact that when the value of δ is small, the Stokes Layer does not interact much with the wall cycle, because it is located very close to the wall only, without affecting those structures that are most likely responsible for turbulent production. At the same time, when the period T is very small, it does not interact with the regeneration cycle of turbulent structures at wall. This might explains why in both cases there appears to be a certain independence of DR with respect to the forcing parameters.
Based on the information presented in Figure 4a, it is possible to divide the forcing velocity profiles (Eq. (4)) into three different groups depending on the value of δ that characterizes them. The first group, characterized by $0 \leq \delta^+ \leq 4$, produces values of DR that appear to be independent of the T^+ parameter. This suggests that in the very near-wall zone there are turbulent structures that are particularly independent to changes of the oscillation rate, and that any Stokes layer temporal oscillation (with $0 \leq \delta^+ \leq 4$) is sufficient to result in a DR of approximately $10 - 15\%$. Then there is the second group, with δ^+ between 4 and 10, for which DR depends on the considered parameter T^+ , but still guarantees higher DR with increasing δ^+, for a fixed T^+. In this case, regardless the oscillation period, increasing the thickness of the Stokes Layer, while remaining in the aforementioned zone, results in a positive effect on DR for all temporal variations driven by T^+. Finally, the last group of forcings, characterized by $\delta^+ \geq 10$, act on a wall-normal region that is highly sensitive to the specific value of T^+. In this case, it is only beneficial (until $\delta^+ \leq 14$) to have a thick Stokes layer if T^+ is close to T^+_{opt}, whereas it can be completely counterproductive in the case of slow oscillations, even leading to drag increase for the $(T^+, \delta^+) = (200, 20)$ case. As discussed later in Section 3.2, it appears that creating a thick Stokes layer with slow oscillations leads to an increase in sweep and ejection events, effectively increasing the phenomena characterized by vertical velocity fluctuations.
The results presented in Figure 4b confirm the observations made from Figure 4a, but with the variables T and δ scaled using the viscous velocity u_τ associated with drag reduced flow. It's worth noting that there is not necessarily one scaling approach that is superior to another, as each provides a different perspective on the same results. Nevertheless, the qualitative information obtained from these two approaches is quite similar. For example, T^*_{opt} remains in the range of $T^* = 30 - 40$, which is markedly different from the classic results obtained with oscillating walls (see Section 1). In general, T^* remains the dominant parameter, except for thin Stokes layers where changes in the velocity profile height have a significant impact. When $T^* \geq 50$ and $4 \leq \delta^* \leq 10$, it appears that $(\partial DR/\partial \delta^*) = 0$. However, this effect is likely due to the lack of discrete results in this region, which makes it challenging to obtain a uniform data grid. In fact, determining the particular pair of (T^*, δ^*) requires first finding the C_f and u_τ.

3.2. Reynolds stresses

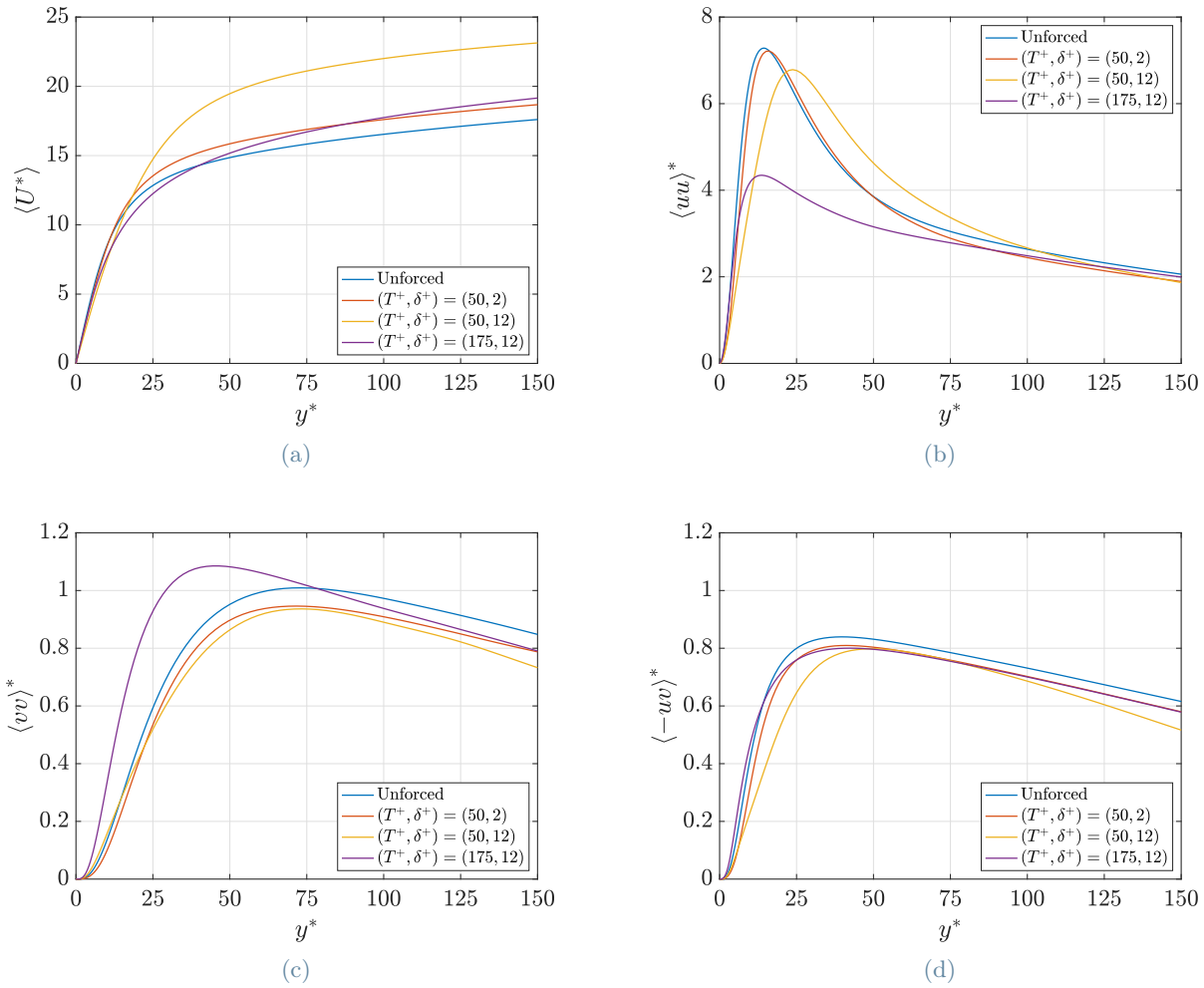

Figure 6: Wall normal profile of mean streamwise velocity and Reynolds stresses (at Nominal $Re_\tau = 400$ and $A^+ = 12$):(a) U^*; (b) $\langle uu \rangle^*$; (c) $\langle vv \rangle^*$; (d) $\langle -uv \rangle^*$

.

All variables shown in this analysis are scaled in actual viscous units, therefore considering each case with respect to its viscous units. Applying scaling based on the actual friction velocity u_τ enables proper non-dimensionalization of the mean flow close to the wall. This facilitates comparison between the drag-reduced statistics in the near-wall region and the statistics of unactuated turbulent flow at the same friction Reynolds number Re_τ. All quantities enclosed in the $\langle \cdot \rangle$ brackets are temporally and spatially averaged along the homogeneous x and z directions.
In order to find a physical explanation to the results we have just shown, it is interesting to observe how the Reynolds stresses behave under different forcing condition with respect to the reference unforced case. We will analyze three different forcing cases, corresponding to three different (T^+, δ^+) pairs, appropriately chosen: $(50, 2)$, $(50, 12)$, and $(175, 12)$, which result in a drag reduction percentage of $10.5\%, 39.4\%$, and 13.8%, respectively. The general transport equation of the Reynolds stress $\langle u_i u_j \rangle$ is defined as

$$\left(\frac{\partial}{\partial t} + U_k \frac{\partial}{\partial x_k} \right) \langle u_i u_j \rangle = P_{ij} - \varepsilon_{ij} + \Pi_{ij} + D^\nu_{ij} + D^p_{ij} + D^t_{ij} \tag{5}$$

where the terms on the right-hand side are the production (P_{ij}), viscous dissipation (ε_{ij}), pressure–strain correlation (Π_{ij}), viscous diffusion (D^ν_{ij}), pressure transport (D^p_{ij}) and turbulent transport (D^t_{ij}). The exact mathematical definition of each right hand side term of Reynolds' stresses equation can be found in [30]. The indices i, j and k can range from 1 to 3 and correspond to the streamwise x, wall-normal y, and spanwise z directions, respectively.

It is known that the main driver of turbulence is the mutual interaction between streaks and QSVs, which support and feed each other, forming the well-known wall cycle [23]. Focusing initially on diagonal Reynolds stresses, it is acknowledged that the major contributions to $\langle uu \rangle$ come from wall streaks, while higher values of $\langle vv \rangle$ and $\langle ww \rangle$ can be linked to a higher intensity of QSVs.

Starting from the analysis of the streamwise Reynolds stress, from Fig. 6b we can notice that the $\langle uu \rangle^*$ massively decreases throughout the height of the channel for the forcing at $(T^+, \delta^+) = (175, 12)$ (except for $y^* \leq 5$), while it is only partially reduced by the $(50, 12)$ and $(50, 2)$ forcing cases, with respect to the reference case. This might suggest that streaks are weakened more in the case of forcing at $T^+ = 175$ compared to the other cases, which seems contradictory since the best DR result is achieved at $T^+ = 50$. Anyway, a similar behavior of $\langle uu \rangle^*$ was observed by [47] for two oscillating wall cases at $T^+ = 100$ and $T^+ = 200$, where the streamwise stress peak near the wall was lower in the latter case than in the former, even though $T^+ = 100$ gave the best DR result. They have shown that this phenomenon is directly proportional to T^+ and therefore not entirely attributable to DR, and this seems confirmed also by our analysis.

On the other hand, the thickening of the viscous sublayer is actually one of the key factor associated with drag reduction, as highlighted by [3]. This phenomenon can be observed from the shift of the peak of $\langle uu \rangle^*$ towards higher y^* values (Fig. 6b). The thickening of the viscous sublayer is also fully confirmed by the analysis of the wall-normal behavior of the mean longitudial velocity $\langle U^*(y^*) \rangle$ shown in Fig. 6a, where it can be seen that its linear near-wall trend extends to higher values of y^* for the forcing that ensures a better DR value. Consequently, the present results provide further evidence that an increase in DR is connected to a thickening of the viscous sublayer, regardless of the values of the two parameters in the Stokes layer, T and δ. Specifically, the observed thickening cannot be solely attributed to either T or δ, as exemplified by the cases of $(T^+, \delta^+) = (50, 2)$ or $(T^+, \delta^+) = (175, 12)$, respectively. However, we did find a significant thickening effect for the combination of $T^+ = 50$ and $\delta^+ = 12$, which represents the most effective friction reduction forcing.

Figure 6c illustrates the variation of $\langle vv \rangle^*$ along the wall-normal direction, which reflects the strength of QSVs and ejections/sweeps phenomena intensity. While the weakening of these structures is evident in the case of $T^+ = 50$ forcings, this is not observed for the one at $T^+ = 175$. Instead, there is even an increase in $\langle vv \rangle^*$ for $y^* \leq 75$ compared to the unforced case.

The aforementioned behavior can be clarified by examining the results presented in Figures 7a, 7b, and 7c, which illustrate the redistribution of normal Reynolds stresses resulting from the pressure-strain correlation terms. These terms are responsible for the energy transfer between diagonal Reynolds stresses due to the effects of pressure-strain interactions, and determine their relative magnitudes. Specifically, when $\Pi_{ii} < 0$, energy is transferred from $\langle u_i u_i \rangle$ to the other diagonal Reynolds stresses, and vice versa when $\Pi_{ii} > 0$. The sum of the diagonal redistribution terms is always zero ($\Pi_{11} + \Pi_{22} + \Pi_{22} = 0$). This means that any increase in the normal stresses due to the pressure-strain correlation is accompanied by a decrease in the other normal stress component.

The behaviour of Π^*_{11} (Fig. 7a) shows that there is no inhibition of energy exchange between the streaks and QSVs in the cases of $(50, 12)$ and $(175, 12)$ forcings. Instead, even more energy is transferred from $\langle uu \rangle^*$ towards $\langle vv \rangle^*$ and $\langle ww \rangle^*$ (because of a more pronunced negative peak). The difference between these two forcings in the redistribution patterns can be easily identified by examining Π^*_{22} and Π^*_{33} curves (Figures 7b and 7c). In comparison to the unforced case, two opposite behaviors are observed: for the $(50, 12)$ forcing, most of the energy seems to follow a preferential path from $\langle uu^* \rangle$ to $\langle ww \rangle^*$, while the opposite behavior is observed for the $T^+ = 175$ forcing, where a lot of energy goes from $\langle uu^* \rangle$ to $\langle vv \rangle^*$, since Π^*_{22} dominates and Π^*_{33} even shows a negative peak, suggesting that some energy is also transferred from $\langle ww \rangle^*$ to the wall normal stress $\langle vv \rangle^*$. At this point, the reason for the greater value of $\langle vv \rangle^*$ for the $T^+ = 175$ forcing can be somehow supported by evidence from the budget terms Π_{ii}.

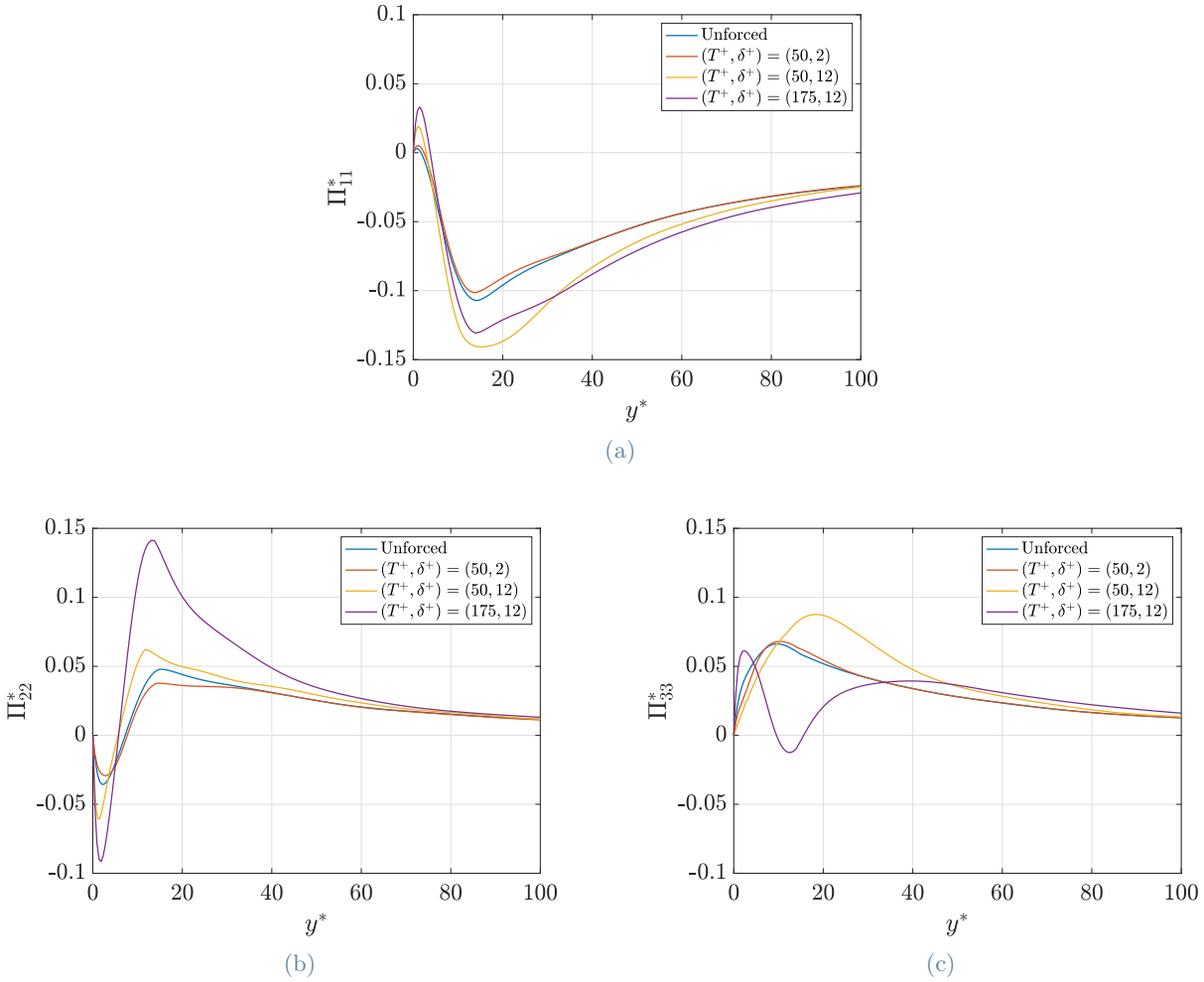

Figure 7: Wall normal profiles of pressure-strain correlation terms (at Nominal $Re_\tau = 400$ and $A^+ = 12$): (a) Π^*_{11}; (b) Π^*_{22}; (c) Π^*_{33}.

The observation of an increased energy exchange from $\langle uu^* \rangle$ to $\langle vv^* \rangle$ when $T^+ = 175$, provides evidence that there is no inhibition of the vertical fluctuating velocity field. On the contrary, our findings suggest that sweep and ejection events may be enhanced by slow-oscillations of the Stokes layer.
The wall-normal Reynolds stress is a very important quantity, since it is primarily responsible for the production of the shear stress $\langle -uv \rangle^*$ (shown in Figure 6d) through the production term $P_{12} = \rho \langle vv \rangle \frac{dU}{dy}$. Similarly, $\langle -uv \rangle$ comes into play in the production of $\langle uu \rangle$ through $P_{11} = -2\rho \langle uv \rangle \frac{dU}{dy}$, thus completing the wall cycle through the influence of QSVs on the wall streaks.
Finally, taking a step back and looking at the near-wall peak of $\Pi^*_{11} \geq 0$ for the $T^+ = 175$ forcing (Fig. 7a), it is very clear how the trend of redistribution of diagonal Reynolds stresses (this time towards $\langle uu \rangle$) increases and not just a little, even compared to the unforced case: this once again demonstrates how forcings with periods far from optimal induce greater energy exchange from $\langle vv \rangle$ and $\langle uu \rangle$, and vice versa (Fig. 7b).
In summary, a main aspect can be inferred from this analysis: a Stokes layer with a period T far from the optimal one causes an energy exchange activity between longitudinal and wall normal Reynolds stresses, that exceeds the one of the reference flow, as we have seen through the graphical representations of the Reynolds stress budget terms. Although not confirmed by the observations of the case $(T^+, \delta^+) = (175, 12)$, this could explain why, in some cases, a drag increase situation has also been found. Increasing δ beyond the optimal value leads to a loss of maximum effectiveness in weakening the streaks, which, together with an excitation of the streaks-QSVs bond due to a non-optimal T, can lead to a consequent increase in skin-friction drag.

4. Lagrangian tracers

To better understand the flow behavior with respect to different pairs of (T^+, δ^+), an analysis using tracer particles is now considered. The objective is to establish a relationship between the parameters of the Stokes layer and the resulting DR value.

In order to gain fundamental knowledge about fluid particle-tracer interaction and accurately predict velocity fluctuations, it is useful to examine the statistical properties of particle motion. The Lagrangian frame of reference is particularly effective in computing statistical properties, as highlighted by previous research conducted by [46] and [45]. With the advent of Direct Numerical Simulations (DNS) of turbulent flows, it has become much easier to extract Lagrangian turbulence statistics by tracing fluid particles. These simulations provide instantaneous realizations of turbulent fields, allowing researchers to investigate particles trajectories with varying levels of complexity. These particles can be ideal tracers without mass or have finite mass, which makes inertia important in determining their trajectories.
[48] and [2] computed Lagrangian statistics from DNS of a turbulent channel flow, focusing on the interpolation method of tracers' velocity field. In fact, a critical part of particles tracking calculations, which becomes the sole issue when particles are massless (tracers), is the interpolation required to obtain the particle velocity from known values of the Eulerian velocity field. Several works compared and evaluated different interpolation schemes, as [8] and [15].
The relative dispersion of two particles has been the first statistic studied quantitatively in turbulent flows. This was initially investigated by [43], in the context of dispersion in the atmosphere. Later, the concept was revisited by [4], also thanks to Kolmogorov's 1941 theory on isotropic turbulence [12]. In the context of two-particle dispersion problems, nowadays the literature on Lagrangian properties of particles in turbulence is extensive [5, 6, 33].
In [32], anisotropy investigation of Lagrangian statistics is presented, with a focus on dispersion when shear separation effect is removed. This work has shown the shear separation effects on particle dispersion, identifying how the dynamics of pair separation has different characteristics in each flow direction due to the presence of shear in the mean velocity field. The particles dispersion is defined as the mean square separation $\overline{d(t)^2} = \overline{\mathbf{d}(t) \cdot \mathbf{d}(t)}$, where $\mathbf{d}(t) = \mathbf{x}_p^{P_1}(t) - \mathbf{x}_p^{P_2}(t)$ represents the separation vector between two paired particles P_1 and P_2, and $\mathbf{x}_p^i(t)$ represents the position of the i-th particle at time t, while the overbar indicates the averaging operation over all particle pairs.
It is interesting to investigate how the relative dispersion between pairs of particles $\overline{d(t)^2}$ is influenced by the Stokes layer generated by wall movement. This is useful to understand how near-wall fluid particles are influenced by the transverse velocity profile (Eq.(4)). Indeed, a possible explanation for the phenomenon of friction reduction through wall oscillation is that the wall cycle formed by the reciprocal interaction between wall streaks and QSVs is somehow shielded by the Stokes layer.
The concept of shear sheltering as a possible explanation for the DR mechanism is not new. It was first introduced in [20], in the context of the continuous spectrum of the Orr-Sommerfeld equation. Generally, it is defined as the effect of the mean flow velocity profile in a boundary layer on turbulence [22]. [35] attempted to establish a relationship between this phenomenon and a decrease in skin-friction drag caused by polymers. They discovered that the introduction of polymers reinforces the shear sheltering mechanism, which produces a blocking effect at a certain distance from the wall that prevents large eddies from the channel center to perturbe near-wall zone. Consequently, the wall cycle is damped, and the near-wall turbulence is weakened, resulting in a less intense fluctuating field. If this is true, the turbulent activity within the transverse boundary layer would be inhibited in its velocity fluctuation components, particularly those normal to the wall, which are responsible for sweep and ejection phenomena.

4.1. Particles computational model

After setting the total number of particles n_p to be inserted inside the channel, particles are organized into $n_{group} = n_p/4$ groups of four, as shown in Fig. 8. The first particle of each group, labeled as P_1, is inserted at a specific point $\mathbf{x}_0^{P_1} = (x_0, y_0, z_0)$ in the domain at time $t = 0$, while the other three particles, namely P_2, P_3 and P_4 are introduced at same position but shifted by a certain $d_{0,x}, d_{0,y}$ and $d_{0,z}$, respectively. The initial position $\mathbf{x}_0^{P_1} = (x_0, y_0, z_0)$ and the components of the initial separation vector $\mathbf{d}_0 = (d_{0,x}, d_{0,y}, d_{0,z})$ are freely selectable. Once these two inputs and the total number of tracers as n_p are chosen, the initial arrangement of all particles is fully determined, and therefore the entire process of polynomial interpolation can start.

4.1.1 Interpolation scheme

The numerical method to calculate the instantaneous position of particles is based on the integration of their equation of motion. Since particles are considered ideal and massless, the equation of motion simplifies as:

$$\frac{\partial \mathbf{x}(\mathbf{x_0}, t)}{\partial t} = \mathbf{v}(\mathbf{x_0}, t), \tag{6}$$

where $\mathbf{x}(\mathbf{x_0}, t)$ and $\mathbf{v}(\mathbf{x_0}, t)$ are respectively the instantaneous position and velocity of the fluid particle identified by the position vector $\mathbf{x_0}$ at time $t = 0$.

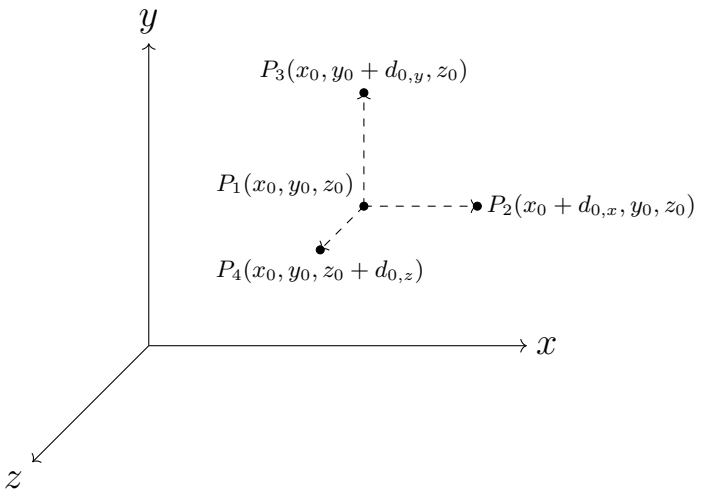

Figure 8: Initial positioning of a group of particles.

The DNS code affords access to the Eulerian velocity $\mathbf{u}(t)$ for each point of a three-dimensional computational grid at every time step. However, it should be noted that the particle's instantaneous position $\mathbf{x}(t)$ often fails to align with a point of the 3D computational grid, and the same holds for its velocity $\mathbf{v}(t)$, which might be different from the grid-point one $\mathbf{u}(t)$. As a result, proper interpolation of the particle's Lagrangian velocity $\mathbf{v}(t)$ from the discrete velocity field of the turbulent flow $\mathbf{u}(t)$ is needed.
Accurately modeling particle trajectories in turbulent flow requires precise interpolation techniques. The Eulerian velocity field's spatial variations make interpolation calculations particularly challenging, as numerical errors can quickly accumulate over time. Turbulent channel flow poses unique challenges, as high-energy small-scale motions are difficult to interpolate, particularly near the walls where periodicity cannot be applied in the y-direction. In this context, higher-order polynomial interpolation is limited to particles within $(n/2-1)$ grid points off the wall, where n is the interpolating polynomial's order. However, the present DNS code's ghost points can extend this range to $(n/2-2)$ grid points, but this is still not optimal, as high accuracy is required near the wall. In our case, to overcome this limitation, a mesh in the wall-normal direction of constant/linear type was adopted: in this way, the wall-normal resolution is arbitrarily reduced with the aim of recovering the interpolation's accuracy where the order of the interpolating polynomial has to be decreased. As the grid spacing h approaches zero, the approximation error decreases asymptotically at a rate of $\mathcal{O}(h^{n+1})$, meaning the achieved approximation is of order $n+1$. Thus, although we must decrease the interpolating polynomial's order, our approach still achieves acceptable resolution while maintaining the necessary accuracy.
In the present work, sixth-order Lagrange polynomials are used as the interpolating function for the discrete velocity field, as they are able to achieve the required sufficient accuracy with minimal computational cost. In order to determine the velocity of a given particle, it is necessary to interpolate the velocity vectors of the nearest grid points. In our DNS code, this velocity field is obtainable after the calculation of nonlinear terms for each time step, since such operation is done in the physical space. Once the real velocity field of the 3D grid is known, the Lagrangian velocity of the particle $\mathbf{v}(\mathbf{x}(t), t)$ is calculated through polynomial interpolation (all details of this method can be found in [15]). From here, the position of the i-th particle can be calculated as follow:

$$\mathbf{x}^i(t+\Delta t) = \mathbf{x}^i(t) + \Delta t \cdot \mathbf{v}(\mathbf{x}^i(t), t), \tag{7}$$

where Δt is the chosen time step. In the present case, the temporal advancement method is the third-order Runge-Kutta method, which specifies three sub-iterations to be performed for each Δt based on certain progression coefficients. This means that for every time step, the simulation actually performs three sub-iterations to obtain the desired temporal accuracy. At this point, after calculating the Lagrangian position and velocity vectors for each particle, the resulting data is stored, allowing the computation of statistics using dedicated post-processing codes.

4.1.2 Method validation

This paragraph describes the validation process for the employed interpolation and post-processing code, as discussed in 4.1.1. As previously stated, [32] provides a comprehensive database of relative dispersion for

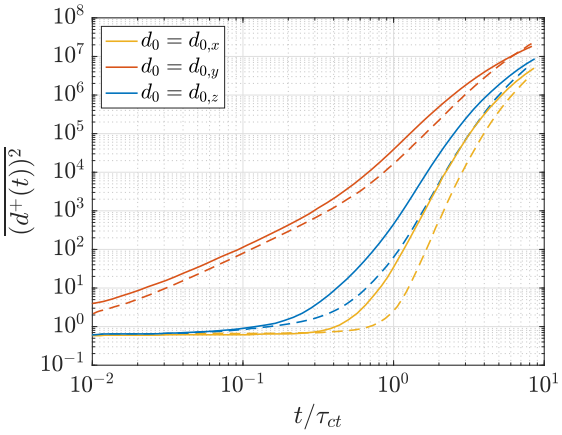

Figure 9: Time evolution of mean-square separation, $\overline{(d^+(t))^2}$ for tracer pairs. Different colors stands for pairs with initial separation vector oriented in streamwise ($d_0 = d_{0,x}$), wall-normal ($d_0 = d_{0,y}$), and spanwise ($d_0 = d_{0,z}$) directions. Solid lines depict the results of the present study, while dashed lines represent the results from [32].

turbulent channel flow. Unlike the last validation (Section 2.3), no particles simulation is conducted to compare the literature results under identical conditions.
The difference between the case in [32] and the current work is the friction Reynolds number, which is $Re_\tau = 150$ for the former and $Re_\tau = 200$ for our simulation. In both works, particle pairs are released at an injection height of $y_0^+ = 2$ and with an initial separation vector of $d_0^+ = 0.76$ or $d_0 = 0.005h$ in all three directions, with h being half channel height. The results are presented with the horizontal axis representing time evolution normalized with respect to the crossing time τ_{ct}. This variable is defined as the time required for a fluid particle positioned at the center of the channel to cover one channel length L_x at a velocity of u_{cl}.
In Figure 9 the results of the described validation are shown, comparing the time evolution of the mean-square separation $\overline{(d^+(t))^2}$ for different particles pairs. Despite the presence of minor quantitative variations, the overall results are deemed satisfactory, given the discrepancy in Re_τ, the use of a different DNS solver, and the distinct approach to interpolate the particles velocity $\mathbf{v}(t)$.

4.1.3 Simulation parameters

The DNS are conducted under Constant Flow Rate (CFR) conditions at $Re_\tau = u_\tau h/\nu = 400$ (as for the simulations described Section 2.1). The computational box size is $(L_x, L_y, L_z) = (4\pi h, 2h, 2\pi h)$, discretized with $N_y = 300$ grid points in the wall-normal direction y and $N_x = 512$ and $N_z = 256$ Fourier modes in the x and z directions, respectively, with an additional factor of 3/2 to eliminate aliasing error. The streamwise and spanwise resolutions are approximately $\Delta x^+ = \Delta z^+ \approx 6.5$. The wall-normal mesh is a constant-linear node distribution, maintaining $\Delta y^+_{min} = 0.5$ until $y^+ < 25$, beyond which Δy^+ increased linearly until it reached $\Delta y^+_{max} \approx 6.2$ at the channel centerline. The low near-wall resolution $\Delta y^+_{min} = 0.5$ is chosen to maintain an optimal accuracy of the interpolation of the particles' velocity field (as described in sec 4.1.1), as well as to more accurately represent the transverse velocity profile dictated by the Stokes layer.
The main particles' analysis is composed of 16 forced simulations, which are performed for different combinations of the Stokes layer parameters, namely (T^+, δ^+). Among these, 9 simulations were carried out with $T^+ = 50$, and δ^+ was varied between 2 and 18 with a step size of 2. The remaining 7 simulations were performed with a constant value of $\delta^+ = 12$, while T^+ was varied between 25 and 175 with a step size of 25, plus a simulation with $T^+ = 10$.
In this context, a total of $n_p = 2.2 \cdot 10^6$ particles are released randomly on a plane parallel to the wall for each simulation, in such a way that the entire x-z plane is adequately filled with a sufficient number of tracers, representing a high percentage of the flow elements. Particle pairs are injected at a release height of y_0^+ with an initial separation of $\mathbf{d}_0$ in various directions. The wall-normal injection height of the particles has been set to $y_0^+ = \delta^+/2$ for each forced simulation, while in the reference case $y_0^+ = 6$. The magnitude of the initial separation vector $\mathbf{d}_0$ has been kept constant at $d_0^+ = 0.76$ or $d_0 = 0.019h$ in all directions.
The temporal evolutions of the results will be visualized through the normalized time t with respect to the crossing time τ_{ct}, which in the current simulations (expressed in nominal viscous units) is equal to:

$$\tau^+_{ct} = \frac{L^+_x}{u^+_{cl}} = \frac{5026.54}{20.08} \approx 250, \tag{8}$$

where u_{cl}^+ is the longitudinal velocity at channel centerline. To collect statistical data and perform ensemble averaging, a time window of duration ΔT^+ was used. This time window is expressed in terms of the number of crossing times τ_{ct}^+, and is equal to $\Delta T^+ = 8.5\tau_{ct}^+$.

5. Particles results

5.1. General particles behaviour

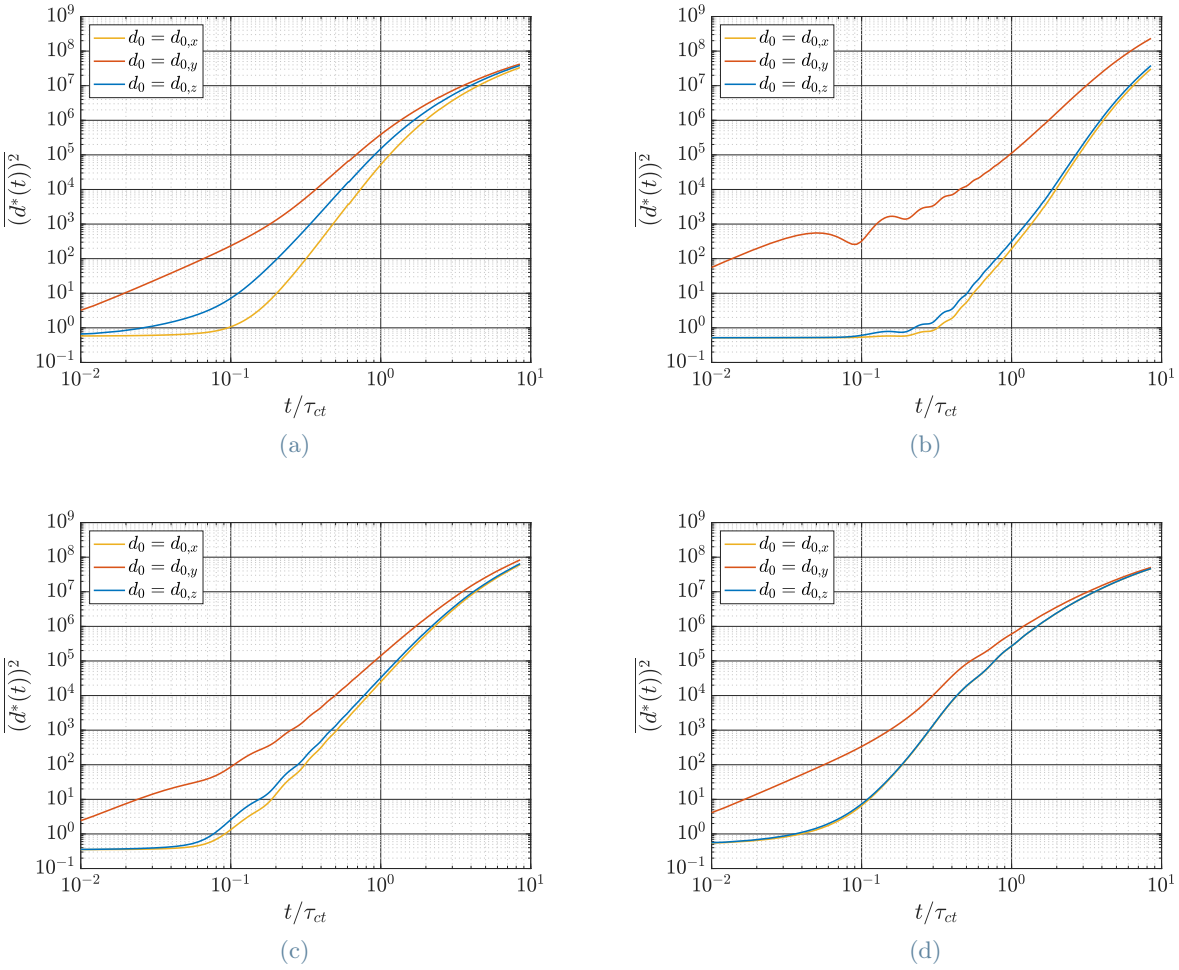

Figure 10: Time evolution of the mean-square separation $\overline{(d^*(t))^2}$ for tracer pairs: (a) unforced reference case, (b) forced case with $(T^+, \delta^+) = (50, 2)$, (c) forced case with $(T^+, \delta^+) = (50, 12)$, (d) forced case with $(T^+, \delta^+) = (175, 12)$.

In order to understand the differences in flow behavior in forced simulations compared to the reference case, the relative dispersion $\overline{d(t)^2}$ (introduced and described in Section 4) is used. Particles pairs are initially organized as described in Section 4.1: for each n_{group}, 12 different dispersions can be examined. Specifically, three pairs of particles with different initial separations based on the direction of $\mathbf{d}_0$ are considered. For each pair, particles' distance can be calculated as absolute $\overline{d(t)}$ or relative to one of the three directions, namely $\overline{d_x(t)}, \overline{d_y(t)}$, or $\overline{d_z(t)}$. This yields to 12 different combinations based on the initial separation and direction of distance considered.
Figure 10 shows time behavior of the mean square separation $\overline{(d^*(t))^2}$ (scaled in actual viscous units) of three different particle pairs, initially separated with separation vector oriented in the streamwise ($d_0 = d_{0,x}$), wall-normal ($d_0 = d_{0,y}$), and spanwise ($d_0 = d_{0,z}$) directions, respectively (consistently with the initial pairs arrangement shown in Fig. 8). In order to examine the effects of different $W(y,t)$ (Eq. (4)) on flow behavior, three different pairs of (T^+, δ^+) were considered in addition to the unforced reference case. Specifically, for Figures 10b, 10c, and 10d, the forcing profiles correspond to $(50, 2)$, $(50, 12)$, and $(175, 12)$, which result in a drag reduction percentage of $10.5\%, 39.4\%$, and 13.8%, respectively.

The effect of flow anisotropy can be observed in Fig. 10, for all flow conditions. It is evident that particle pairs with a wall-normal initial separation $d_{0,y}$ exhibit a greater dispersion compared to those with initial separation in homogeneous directions $d_{0,x}$ and $d_{0,z}$. This behavior can be attributed to high local gradient $\partial U/\partial y$ of the mean flow velocity, which immediately increases the distance between particles in the streamwise direction and decorrelates the longitudinal velocities of the particles pair. This is evident for both reference (Fig. 10a) and forced cases with injection height $y_0^+ = 6$ (Figures 10c and 10d), but when particles' injection height is even closer to the wall (i.e., $y_0^+ = \delta^+/2 = 1$ as in Fig. 10b), the effect of wall anisotropy is even more pronounced, with large differences depending on the orientation of the initial separation vector $\mathbf{d}_0$.
In drag reduced flow, it is very interesting to observe the overlap of $\overline{(d^*(t))^2}$ for pairs of particles with initial separation in the two homogeneous directions $d_{0,x}$ and $d_{0,z}$. This happens because particles at the same height y experience the same mean longitudinal velocity $U(y)$ and transverse velocity $W(y)$ of the Stokes layer. As a result, it is reasonable to assume that the Stokes layers level the behavior of fluid particles within wall-parallel $x^+ - z^+$ planes at a fixed height y^+. Essentially, this means that if we could eliminate any vertical fluctuation (preventing wall-normal movement), the relative distance between particles with $d_{0,x}$ or $d_{0,z}$ would remain constant over time.
Additionally, when the flow is spanwise forced by $W(y,t)$ (Eq. (4)) it transfers the oscillatory behaviour to $\overline{(d^*(t))^2}$. This behavior becomes more pronounced when the oscillations are faster (lower T^+) and the particles are released closer to the wall (lower y_0^+), as the spanwise shear $\partial W/\partial y$ increases when y^+ approaches zero.

5.2. Vertical dispersion

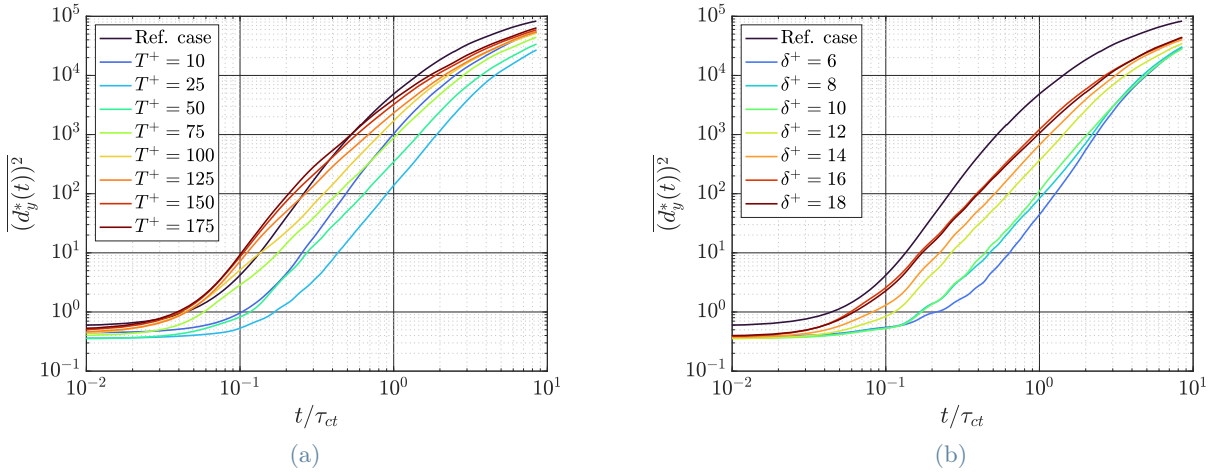

Figure 11: Time evolution of wall-normal relative dispersion due to wall-normal initial separation at different forcing conditions. In (a), the forcings are characterized by the same $\delta^+ = 12$ and different T^+. In (b), the forcings are characterized by the same $T^+ = 50$ and different δ^+. The particles' injection height is equal to $y_0^+ = 6$ for the reference case and $y_0^+ = \delta^+/2$ for the forced cases.

The aim of this particles' study is to investigate whether the shear sheltering effect caused by the Stokes layer is somehow related to the DR provided by the wall motion. In essence, we are investigating whether a more effective Stokes layer, which leads to a higher DR, also results in a more pronounced blocking effect. By examining this potential correlation, our goal is to gain insights into the underlying the mechanisms that drive this phenomenon.
In order to analyze the shear sheltering provided by the Stokes layers (described in Section 1), it is more useful to look at the component of relative dispersion normal to the wall, namely $\overline{d_y(t)^2} = \overline{(y^{P_1} - y^{P_2})^2}$ (where y^{P_1} and y^{P_2} are the wall-normal coordinates of the particles pair), than sticking to mean square separation $\overline{(d^*(t))^2}$.
Figure 11a shows wall-normal relative dispersion $\overline{(d_y^*(t))^2}$ due to wall-normal initial separation ($d_{0,y}^+ = 0.76$) with release height $y_0^+ = 6$ for distinct Stokes layers, specifically characterized by same $\delta^+ = 12$ but different T^+.
In order to clarify its physical meaning, a lower relative vertical dispersion $\overline{(d_y^*(t))^2}$ indicates that a pair of particles tends to slowly vary their relative distance in the y direction.
From Figure 11a, it is immediately noticeable that the great majority of forcing conditions reduce $\overline{(d_y^*(t))^2}$ compared to the unforced reference case.
Essentially, the optimal T^+ order found in the drag reduction analysis (conducted in Section 3) is confirmed.

Specifically, the minimum average vertical dispersion is obtained for $T^+ = 25$, followed by $T^+ = 50$ case. This suggests that at these oscillation periods, the Stokes layer is highly effective in reducing vertical fluctuations, resulting in the inhibition of turbulent phenomena such as sweeps and ejections.
Furthermore it is evident that moving away from the optimal $T^+ = 25 - 50$, results in a decrease in screening action compared to oscillations with faster temporal variations. Notably, for all forcings with $T^+ \geq 125$ for $t \leq 0.2\tau_{ct}$, the vertical dispersion $\overline{(d_y^*(t))^2}$ is even greater than the unforced reference case. Surprisingly on one hand, it is interesting to remember the behavior of the wall-normal Reynolds stress $\langle vv \rangle^*$ shown in Fig. 6c. Indeed, for $(T^+, \delta^+) = (175, 12)$, $\langle vv \rangle^*$ at $y^* = y_0^+ = 6$ was higher than the unforced case, indicating that the intensity of wall-normal fluctuations was not attenuated by the forcing, but rather amplified. The analysis of the budget terms of the Reynolds stress equations revealed that the slow oscillations of the Stokes layer alter the energy redistribution among the diagonal stresses. Specifically, they increase the direct energy transfer from $\langle uu \rangle^*$ and $\langle ww \rangle^*$ to $\langle vv \rangle^*$. It is presumed that these two effects are correlated, and this connection can explain the lower shear sheltering effect guaranteed by high-T^+ forcings.
As for the behavior of the Stokes layer at $T^+ = 10$, we notice how it initially appears particularly effective, but it then results in a $\overline{(d_y^*(t))^2}$ with the highest growth rate over time. Although the reasons for this phenomenon are difficult to identify, this confirms that there are optimal T^+ values that provide better shear sheltering effect than others, and that Stokes layers oscillations that become increasingly rapid do not necessarily reduce $\overline{(d_y^*(t))^2}$.
From this analysis, a possible link between DR and shear sheltering effect clearly emerges, since the T_{opt}^+ found in the analysis in Section 3.1 is close to the T^+ values that ensure a lower vertical dispersion of the particles.
Obviously, as t tends to infinity, it is expected that the vertical dispersions, regardless of the characteristics of the forcing, converge to the same value. From this point of view, it is clear that $\overline{(d_y^*(t))^2}$ cannot grow without limits, being limited by geometric constraints such as the lower and upper walls.
Present results indicate that $\overline{(d_y^*(t))^2} \approx 10^5$ at higher t, namely $\overline{d_y^*(t)} \approx 300$. This asymptotic value is much lower than the theoretically achievable one ($d_y^{max} = 2 \cdot Re_\tau = 600 - 800$, depending on the actual Re_τ) and seems to suggest that the final distribution of particle pairs is preferably confined within half of the channel.
In Figure 11b, the parameter being changed for the Stokes layers is its thickness δ^+, while T^+ remains constant at 50. It is important to remember that, prior to the analysis, it was decided to keep $\delta/y_0 = 2$ constant. Therefore, the $\overline{(d_y^*(t))^2}$ curves in Fig. 11b correspond to different injection points y_0^+.
Nonetheless, it can be stated that regardless of y_0^+, inserting particles in the middle of a Stokes layer with $T^+ = 50$ always reduces their tendency to move freely in the wall-normal direction, with respect to the unforced case. This reduction is not proportional to δ/y_0, otherwise we would have seen an overlap of the curves. Consequently, the differeces in the $\overline{(d_y^*(t))^2}$ behaviour between different forcing may be attributed to δ^+ or y_0^+.
The analysis conducted in Fig. 11a has shown that a decrease in $\overline{(d_y^*(t))^2}$ is somehow linked to the effectiveness of the forcing in reducing friction. This suggests that y_0^+ should be the key factor. In fact, the maximum drag reduction is achieved for the velocity profile imposed by $W(y,t)$ with $(T^+, \delta^+) = (50, 12)$. Therefore, if the decrease in $\overline{(d_y^*(t))^2}$ were primarily dependent on the value of δ^+, this forcing should ensure the lowest values of $\overline{(d_y^*(t))^2}$. However, this is not the case, leading to the suspicion that the true difference is made by y_0^+. Indeed, smaller values of y_0^+ guarantee lower $\overline{(d_y^*(t))^2}$ values, as shown in Fig. 11b.

5.3. Snapshots of particles position

Previous analyses on particle dispersion, while very useful in highlighting the effects of forcings on flow behavior, have some limitations.
Specifically, the behavior of $\overline{d^2(t)}$, analyzed in Section 5.1, only allows for general conclusions to be drawn without going into detail on the blocking effect of vertical movements.
On the other hand, $\overline{(d_y^*(t))^2}$ provides insights into the relative behavior between pairs of particles, which is informative about the effectiveness of Stokes layers as the T^+ parameter varies, but is unable to provide an absolute picture of the influence of a Stokes layer in limiting the vertical movements of fluid elements, since only the relative behaviour is taken into account.
In order to overcome these possible limitations, in Fig. 12 the instantaneous distribution of particles in the longitudinal plane $x^+ - y^+$ is shown at time instant $t = \tau_{ct}$ (injection vertical point is $y_0^+ = 6$). This allows for a direct comparison between the unforced reference case and the forced cases with increasing T^+ and same $\delta^+ = 12$.
These snapshots of particles' positions underline once again how differences in the T^+ parameter of the Stokes layer have an impact on the wall-normal behavior of fluid particles. In the forced cases with $T^+ = 25$ and $T^+ = 50$, the effectiveness of the Stokes layer in trapping particles within itself is particularly evident when compared to the reference case and to slower Stokes layers with all other values of T^+.
Even though all forced cases have an identical transverse boundary layer in their wall-normal spatial behavior

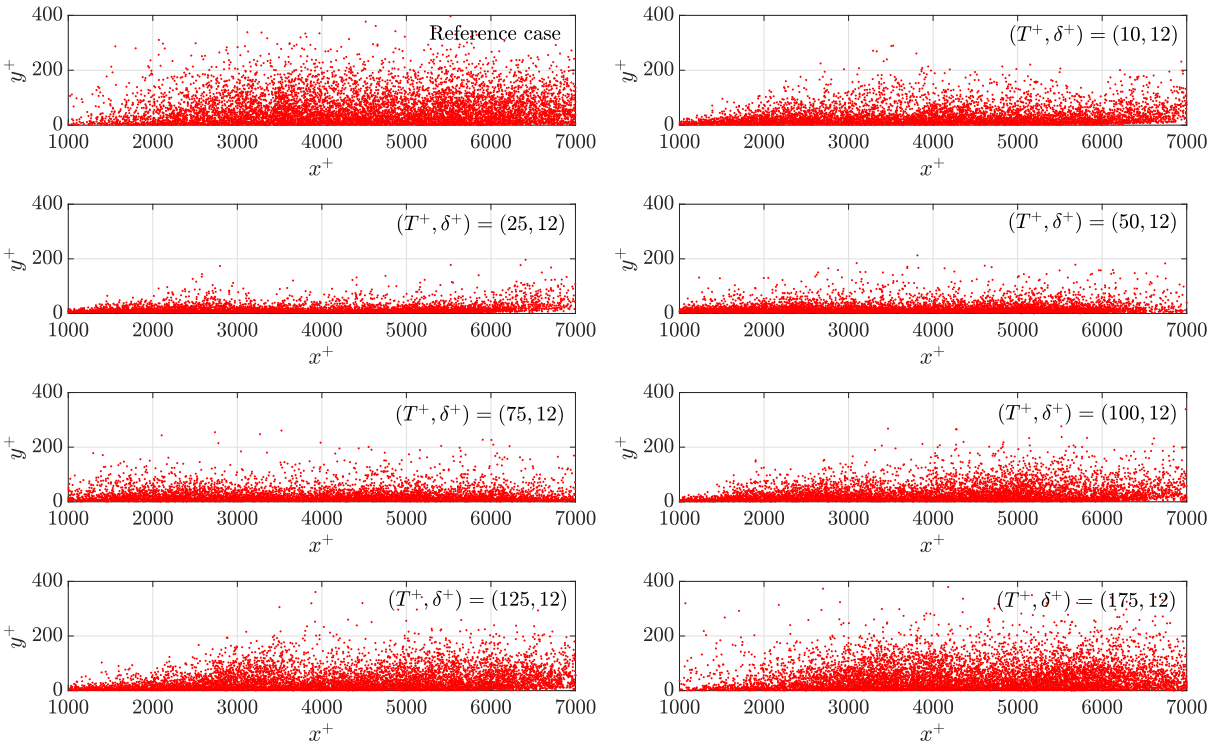

Figure 12: Instantaneous particles position at $t = \tau_{ct}$ for different forcing conditions. Particles have been injected at $y_0^+ = 6$ at $t = 0$.

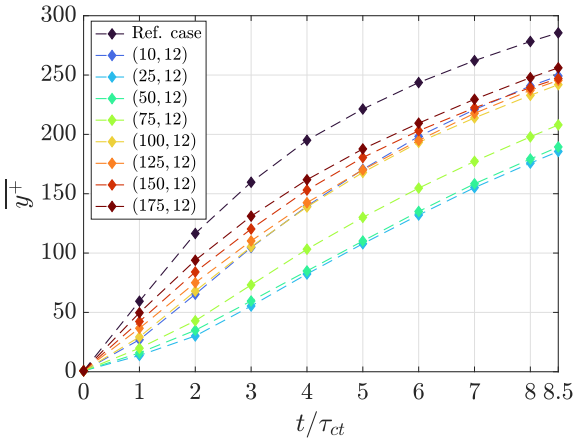

Figure 13: Time variation of the average wall-normal position of all injected particles for different forcings.

(since $\delta^+ = 12$ is the same), it is clear that in the case where $T^+ \approx T^+_{opt}$, shear sheltering is very effective, which strongly limits the vertical movement of fluid particles due to induced shear stress.
The qualitative results obtainable from the observation of Fig. 12 are fully confirmed quantitatively by the data presented in Figure 13, which shows the average $\overline{y^+}$ position of the particles as a function of time for all forcings at the same $\delta^+ = 12$ and different T^+.
After $t = \tau_{ct}$, $\overline{y^+}$ for $T^+ = 25$ and $T^+ = 50$ settles at values of 14 and 15 respectively, whereas the reference case provides $\overline{y^+} = 60$. This indicates that, on average, the particles are distributed closer to the wall by about 75% when subjected to the shear induced by the Stokes layer, which therefore has a massive influence on the wall turbulence.
As T^+ increases, the effect of shear sheltering persists, albeit to a lesser extent, as the oscillations of the Stokes layers become slower. This is evident both visually and quantitatively, as shown in Fig. 12 and Fig. 13, respectively.
In general, even in this latest analysis, it emerges that the T^+ values that better limit vertical movements are the same ones that guarantee a better DR. A great difference with the analysis of $\overline{(d^*_y(t))^2}$ (see Fig. 11a) is that there is no forcing that initially makes the particles freer to move in the wall-normal direction than the reference case. This seems to demonstrate that, at least for the investigated range of T^+, every oscillation period of the Stokes layer results in a certain shear sheltering effect on the flow vertical velocity.
Importantly, the real difference between different-T^+ cases is only significant up to $t \leq 3\tau_{ct}$, after which the growth rate of all the curves remains relatively similar. The above statement highlights that the Stokes layer effect has a limited impact on vertical particles movements, only for a certain time interval. Therefore, it should not be regarded as an infinite effect, but rather as an initial constraint on the particles' tendency to move vertically in the channel.

6. Conclusions

This study proposes a novel method to understand skin friction reduction induced by transverse forcing. By decoupling the spatial and temporal variations of the velocity profile into two parameters, δ and T, it is revealed that the temporal variation of the Stokes layer dominates the resulting friction drag reduction, while its wall-normal spatial behavior contributes to a lesser extent.
The main finding is that the optimal value of T^+_{opt} for maximum friction drag reduction is significantly smaller than the traditional value found in wall motion techniques. Previous studies have shown that the value of $T^+_{opt} = 100$ was the best compromise achievable when considering both temporal and spatial contributions. However, if the goal is to identify the optimal temporal pattern for reducing friction, the best period of oscillation appears to be around $T^+_{opt} = 40$.
This work demonstrates that oscillation periods close to T^+_{opt} result in a greater reduction of friction due to an inhibitory effect of the wall-normal velocity fluctuation field, leading to lower sweep and ejection intensity within the Stokes layer. This is evidenced by analysis of Reynolds stresses and observation of tracers behavior. Specifically, the analysis of tracers suggests that the optimal values for the oscillation period T (in terms of the resulting drag reduction) also result in a greater effect of shear sheltering.
Regarding the optimal wall-normal thickness of the Stokes layer to ensure better friction reduction, it is found that there is no fixed value of δ that works better in an absolute way. In fact, the optimal thickness δ_{opt} is found to be variable depending on the particular value of T. However, when the temporal behavior of the velocity profile is optimal, the best drag reduction value is achieved with a Stokes layer thickness of $\delta^+ = 12$.
The findings of this study provide valuable insights into the optimization of future drag reduction strategies, and offer reliable guidelines for a range of active control techniques, despite being limited to the considered type of synthetic forcing. However, while this work has attempted to provide quantitative evidence to justify the results, further research is needed to fully comprehend the underlying reasons behind some of the findings.
There are several potential areas for future research that could enhance our understanding of skin friction reduction induced by transverse forcing. For example, expanding the investigation beyond the Stokes layer to examine the effect of oscillation amplitude on drag reduction, and extending the use of spatial and temporal decoupling to other types of forcing, such as travelling waves, to determine the general applicability of the outcomes.
Moreover, extending this research to more complex flow regimes, such as those with more complex geometries and boundary conditions, would be interesting to assess the practical applicability of the proposed approach. These future studies have the potential to contribute significantly to the advancement of the understanding of the physics of skin friction reduction, and to the development of optimized drag reduction strategies.

References

[1] R. Akhavan, W. Jung, and N. Mangiavacchi. Control of wall turbulence by high frequency wall oscillations. *AIAA Paper 93-3282*, 1993.

[2] S. Balachandar and M. R. Maxey. Methods for Evaluating Fluid Velocities in Spectral Simulations of Turbulence. *Journal of Computational Physics*, 83:96–125, July 1989.

[3] A. Baron and M. Quadrio. Turbulent drag reduction by spanwise wall oscillations. *Applied Scientific Research*, 55:311–326, 1996.

[4] G. K. Batchelor. The application of the similarity theory of turbulence to atmospheric diffusion. *Quarterly Journal of the Royal Meteorological Society*, 77(332):315–317, 1951.

[5] J. Bec, L. Biferale, A. S. Lanotte, A. Scagliarini, and F. Toschi. Turbulent pair dispersion of inertial particles. *Journal of Fluid Mechanics*, 645:497–528, February 2010.

[6] G. Boffetta and I. M. Sokolov. Statistics of two-particle dispersion in two-dimensional turbulence. *Physics of Fluids*, 14(9):3224–3232, September 2002.

[7] J.-I. Choi, C.-X. Xu, and H. J. Sung. Drag reduction by spanwise wall oscillation in wall-bounded turbulent flows. *AIAA Journal*, 40(5):842–850, 2002.

[8] Jung-Il Choi, Kyongmin Yeo, and Changhoon Lee. Lagrangian statistics in turbulent channel flow. *Physics of Fluids*, 16(3):779–793, March 2004.

[9] K.-S. Choi. Near-wall structure of turbulent boundary layer with spanwise-wall oscillation. *Physics of Fluids*, 14(7):2530–2542, 2002.

[10] G. N. Coleman, J. Kim, and A. T. Le. A numerical study of three-dimensional wall-bounded flows. *International Journal of Heat and Fluid Flow*, 17:333–342, 1996.

[11] C.A. Duque-Daza, M.F. Baig, D.A. Lockerby, S.I. Chernyshenko, and C. Davies. Modelling turbulent skin-friction control using linearised Navier-Stokes equations. *Journal of Fluid Mechanics*, 702:403–414, 2012.

[12] U. Frisch. *Turbulence: The Legacy of A. N. Kolmogorov*. Cambridge University Press, November 1995.

[13] D. Gatti and M. Quadrio. Performance losses of drag-reducing spanwise forcing at moderate values of the Reynolds number. *Physics of Fluids*, 25:125109(17), 2013.

[14] D. Gatti and M. Quadrio. Reynolds-number dependence of turbulent skin-friction drag reduction induced by spanwise forcing. *J. Fluid Mech.*, 802:553–58, 2016.

[15] van Hinsberg, M.A.T., ten Thije Boonkkamp, J.H.M., F. Toschi, and H.J.H. Clercx. On the efficiency and accuracy of interpolation methods for spectral codes. *SIAM Journal on Scientific Computing*, 34(4):B479–B498, 2012.

[16] R.J.A. Howard and N.D. Sandham. Simulation and modelling of a skewed turbulent channel flow. *Flow, Turb. Comb.*, 65:83–109, 2000.

[17] E. Hurst, Q. Yang, and Y.M. Chung. The effect of Reynolds number on turbulent drag reduction by streamwise travelling waves. *Journal of Fluid Mechanics*, 759:28–55, November 2014.

[18] N. Hutchins and I. Marusic. Evidence of very long meandering features in the logarithmic region of turbulent boundary layers. *Journal of Fluid Mechanics*, 579:1–28, 2007.

[19] Nicholas Hutchins and Ivan Marusic. Large-scale influences in near-wall turbulence. *Philosophical Transactions of the Royal Society A: Mathematical, Physical and Engineering Sciences*, 365(1852):647–664, March 2007.

[20] Robert G. Jacobs and Paul A. Durbin. Shear sheltering and the continuous spectrum of the Orr–Sommerfeld equation. *Physics of Fluids*, 10(8):2006–2011, July 1998.

[21] J. Jeong, F. Hussain, W. Schoppa, and J. Kim. Coherent structures near the wall in a turbulent channel flow. *Journal of Fluid Mechanics*, 332:185–214, 1997.

[22] Ignacio Jimenez, Stewart Glegg, and William Devenport. The effect of shear sheltering on trailing edge noise. June 2020.

[23] J. Jiménez and A. Pinelli. The autonomous cycle of near-wall turbulence. *Journal of Fluid Mechanics*, 389:335–359, 1999.

[24] Javier Jimenez. Streak-less wall-bounded turbulence. February 2022.

[25] W.J. Jung, N. Mangiavacchi, and R. Akhavan. Suppression of turbulence in wall-bounded flows by high-frequency spanwise oscillations. *Phys. Fluids A*, 4 (8):1605–1607, 1992.

[26] J. Kim, P. Moin, and R. Moser. Turbulence statistics in fully developed channel flow at low Reynolds number. *Journal of Fluid Mechanics*, 177:133–166, 1987.

[27] F. Laadhari, L. Skandaji, and R. Morel. Turbulence reduction in a boundary layer by a local spanwise oscillating surface. *Physics of Fluids*, 6 (10):3218–3220, 1994.

[28] P. Luchini. Introducing CPL. *2012.12143*, November 2021.

[29] P. Luchini and M. Quadrio. A low-cost parallel implementation of direct numerical simulation of wall turbulence. *J. Comp. Phys.*, 211(2):551–571, 2006.

[30] N. Mansour, J. Kim, and P. Moin. Reynolds-stress and dissipation-rate budgets in a turbulent channel flow. *J. Fluid Mech.*, 194:15–44, 1988.

[31] R. Nakanishi, H. Mamori, and K. Fukagata. Relaminarization of turbulent channel flow using traveling wave-like wall deformation. *Int J Heat Fluid Flow*, 35:152–159, 2012.

[32] E. Pitton, C. Marchioli, V. Lavezzo, A. Soldati, and F. Toschi. Anisotropy in pair dispersion of inertial particles in turbulentchannel flow. *Physics of Fluids*, 24(073305):1–26, 2012.

[33] J. I. Polanco, I. Vinkovic, N. Stelzenmuller, N. Mordant, and M. Bourgoin. Relative dispersion of particle pairs in turbulent channel flow. *International Journal of Heat and Fluid Flow*, 71:231–245, June 2018.

[34] S.B. Pope. *Turbulent Flows*. Cambridge University Press, Cambridge, 2000.

[35] P. K. Ptasinski, B. J. Boersma, F. T. M. Nieuwstadt, M. A. Hulsen, B. H. a. a. Van Den Brule, and J. C. R. Hunt. Turbulent channel flow near maximum drag reduction: Simulations, experiments and mechanisms. *Journal of Fluid Mechanics*, 490:251–291, September 2003.

[36] M. Quadrio, B. Frohnapfel, and Y. Hasegawa. Does the choice of the forcing term affect flow statistics in DNS of turbulent channel flow? *Eur. J. Mech. B / Fluids*, 55:286–293, 2016.

[37] M. Quadrio and P. Luchini. Integral time-space scales in turbulent wall flows. *Physics of Fluids*, 15(8):2219–2227, 2003.

[38] M. Quadrio and P. Ricco. Critical assessment of turbulent drag reduction through spanwise wall oscillation. *J. Fluid Mech.*, 521:251–271, 2004.

[39] M. Quadrio and P. Ricco. The laminar generalized Stokes layer and turbulent drag reduction. *Journal of Fluid Mechanics*, 667:135–157, 2011.

[40] M. Quadrio and S. Sibilla. Numerical simulation of turbulent flow in a pipe oscillating around its axis. *J. Fluid Mech.*, 424:217–241, 2000.

[41] P. Ricco and M. Quadrio. Wall-oscillation conditions for drag reduction in turbulent channel flow. *International Journal of Heat and Fluid Flow*, 29:601–612, 2008.

[42] P. Ricco, M. Skote, and M. A. Leschziner. A review of turbulent skin-friction drag reduction by near-wall transverse forcing. *Progress in Aerospace Sciences*, 123:100713, May 2021.

[43] L.F. Richardson. Atmospheric diffusion shown on a distance-neighbour graph. *Proceedings of the Royal Society A*, 110(756):709–737, 1926.

[44] S. K. Robinson. Coherent motions in the turbulent boundary layer. *Ann. Rev. Fluid Mech.*, 23:601–639, 1991.

[45] Juan P.L.C. Salazar and Lance R. Collins. Two-Particle Dispersion in Isotropic Turbulent Flows. *Annual Review of Fluid Mechanics*, 41(1):405–432, 2009.

[46] Federico Toschi and Eberhard Bodenschatz. Lagrangian Properties of Particles in Turbulence. *Annual Review of Fluid Mechanics*, 41(1):375–404, 2009.

[47] E. Touber and M.A. Leschziner. Near-wall streak modification by spanwise oscillatory wall motion and drag-reduction mechanisms. *Journal of Fluid Mechanics*, 693:150–200, 2012.

[48] P.K. Yeung and S.B. Pope. An algorithm for tracking fluid particles in numerical simulations of homogeneous turbulence. *J. Comp. Phys.*, 79:373–416, 1988.

Abstract in lingua italiana

Questo studio si pone l'obbiettivo di migliorare la comprensione del fenomeno di riduzione di attrito turbolento indotto da un forzamento trasversale. La nota tecnica di oscillazione di parete genera uno strato limite trasversale, noto come strato di Stokes, in cui il profilo di velocità è descritto analiticamente dalla soluzione del secondo problema di Stokes. Tuttavia, è molto complicato capire se la riduzione di attrito che ne deriva sia determinata principalmente dalle caratteristiche spaziali del profilo di velocità indotto, o dalla sua variazione temporale, in quanto entrambe sono legate al valore del periodo di oscillazione di parete scelto in precedenza, T. Viene suggerito un nuovo approccio che impone il profilo di velocità trasversale direttamente al flusso. Questo metodo separa le variazioni spaziali e temporali in due parametri: uno che misura lo spessore del profilo di velocità trasversale e un altro che ne rappresenta il periodo di oscillazione temporale. Ciò consente di valutare i due contributi separatamente, acquisendo una comprensione più completa del fenomeno.
Lo studio parametrico DNS rivela che il parametro T dello strato di Stokes è il più influente nella riduzione di attrito, mentre lo spessore del profilo di velocità contribuisce in misura minore. In particolare, il valore ottimale di T che garantisce il massimo valore di riduzione di attrito, risulta inferiore (quasi della metà) del valore tradizionalmente trovato nella classica tecnica di movimento di parete. Inoltre, attraverso lo studio degli sforzi di Reynolds e del moto delle particelle traccianti, al variare dei due parametri T e δ, si è cercato di comprendere perché alcuni profili di velocità risultano più efficaci di altri nel garantire maggior riduzione di attrito. In particolare, è risultato che determinati valori di T detrminano una riduzione delle fluttuazioni di velocità verticali, inibendo così l'attività turbolenta all'interno dello strato di Stokes.

Parole chiave: Riduzione di attrito, forzamento trasversale, strato limite di Stokes, particelle traccianti

Ringraziamenti

Con la realizzazione di questo lavoro, si conclude anche questo capitolo della mia vita. Inizio dicendo che non è stato facile. Tanti sono stati i momenti complicati, difficili. Se ce l'ho fatta, è anche grazie alle splendide persone che mi sono state vicino: chi con un consiglio, chi con un sorriso, chi con un abbraccio. Volevo ringraziarvi sinceramente per tutto il sostegno che mi avete dato.

Innanzitutto, un grazie al Prof. Maurizio Quadrio, a Federica e ad Alessandro, per avermi guidato attraverso questo lavoro di tesi, aiutandomi a dare il meglio di me. Senza il vostro aiuto e sostegno, nulla sarebbe stato possibile.

Un grazie speciale va alla mia famiglia, che è stata la colonna portante su cui costruire questo risultato. In particolare, vi ringrazio per aver sempre creduto in me, spero di avervi reso orgogliosi.

Un grazie alla mia ragazza: so che non è stato facile stare al mio fianco durante questo viaggio, trovarti è stata una fortuna.

Un grazie a tutti i miei amici, a quelli veri. Quelli con cui si può dimenticare tutto, quelli con cui "chi sei" non importa, ma basta esserci.

Andrea